Anisotropic Characterization of Nanocrystalline Alloys for Inductive Power Transfer

ALEXANDER K. BAILEY (Graduate Student Member, IEEE),
WENTING ZHANG (Graduate Student Member, IEEE), **SEHO KIM** (Member, IEEE),
AND GRANT A. COVIC (Senior Member, IEEE)

Department of Electrical, Computer and Software Engineering, University of Auckland, Auckland 1010, New Zealand

CORRESPONDING AUTHOR: ALEXANDER K. BAILEY (e-mail: alexander.bailey@auckland.ac.nz)

ABSTRACT Nanocrystalline alloys are of interest in inductive power transfer (IPT) due to their higher saturation limits, permeability, and thermal conductivity compared to conventional Mn–Zn ferrites. However, due to the higher electrical conductivity of nanocrystalline alloys, they have significant eddy current losses. This article demonstrates a core loss measurement method that considers the anisotropic behavior of fractured and laminated nanocrystalline ribbons. The proposed method uses a Maxwell coil to generate a uniform magnetic field, while samples of nanocrystalline ribbon are mechanically rotated within the magnetic field. Core loss is then measured using a hybrid calorimetric method that combines steady-state and transient measurements, enabling quick and accurate acquisition. The measured core loss of three different nanocrystalline ribbon samples is compared at 85 kHz for IPT applications. Finally, a modified Steinmetz equation dependent on the magnetic flux angle is proposed.

INDEX TERMS Calorimetry, core loss, inductive power transfer (IPT), loss measurement, magnetic losses.

I. INTRODUCTION

Electric vehicles (EVs) are now a viable alternative to light-duty passenger vehicles. Compared to traditional internal combustion engine vehicles (ICEVs), EVs can have significantly lower environmental impacts throughout their lifetime through reduced tailpipe emissions [1]. However, one significant barrier against the widespread adoption of EVs is range anxiety - the concern that an EV's range is smaller than an ICEV.

To combat this, wireless charging of EVs using inductive power transfer (IPT) has been proposed to improve charging convenience, enabling 'power snacking' [2]. In the last decade, industry and research groups have developed IPT systems for passenger EV charging at power levels in the order of 10 kW. However, IPT charging of heavy-duty electric vehicles (HDEVs) such as trucks and buses is also desirable, to reduce emissions further. The heavy-duty charging standard SAE J2954/2 is currently under development and

is expected to require power levels up to 1 MW. To enable IPT charging of HDEVs with reasonable charge times and magnetics dimensions, IPT power levels and power densities must improve. One limiting factor of the IPT magnetics' power density is the magnetic core material. Typically, a core of magnetic material is used to channel magnetic flux behind the coil, improving magnetic coupling and reducing leakage flux as shown in Fig. 1 [3], [4].

Conventionally, Mn–Zn ferrites are used due to their low electrical conductivity and cost. However, Mn–Zn ferrites are mechanically brittle and have undesirable properties such as relatively low Curie temperatures ($\sim 220\,°C$) and saturation flux densities ($\sim 400\,mT$). In practice, Mn–Zn ferrites cannot be operated near $120\,°C$ without issues resulting from thermal runaway as Mn–Zn core loss is positively correlated with temperature above this operating point [5].

Nanocrystalline alloys have the potential to improve the power density and efficiency of IPT systems due to their high
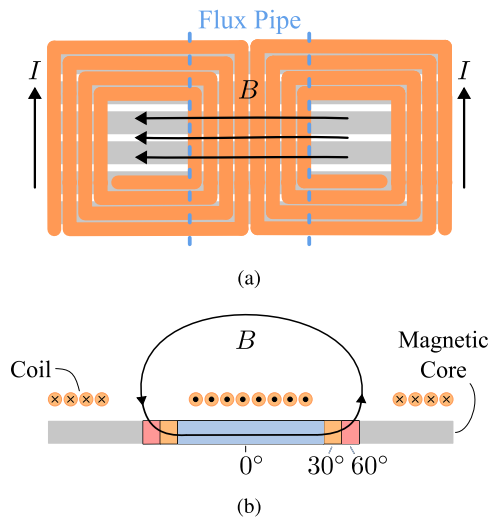
FIGURE. 1. Overview of DD IPT coupler field shape and nonaligned flux in the core (a) Top view of DD IPT coupler, each winding is 180° out of phase, creating a 'polarised' field shape which has a strong horizontal component, (b) Cross-section of DD IPT coupler showing simplified primary magnetic flux path with regions of nonaligned magnetic flux highlighted.
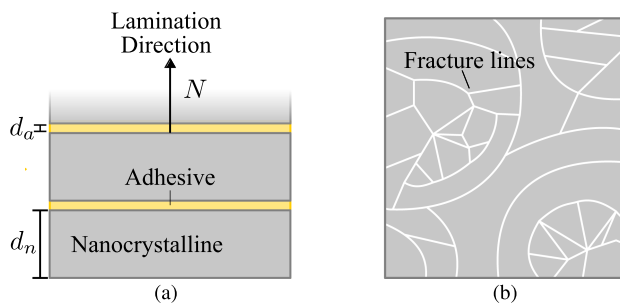

FIGURE. 2. (a) Lamination of N layers of nanocrystalline, (b) Fracturing of nanocrystalline surface.

permeability and saturation flux densities above 1.2 T [6]. However, nanocrystalline alloys are more conductive than Mn-Zn ferrites, leading to higher induced eddy current losses at the 85 kHz operating frequency required by the SAE J2954 standards. Lamination and fracturing are the two primary techniques used to reduce nanocrystalline materials' bulk conductivity and mitigate eddy current losses.

Nanocrystalline ribbons are formed by lamination of thin films as shown in Fig. 2(a). This restricts the path of induced eddy currents in the material, reducing the associated losses. To reduce computational complexity, the literature proposes a homogenization method, where a laminated core is represented by an equivalent anisotropic non-laminated core [7]. High-power IPT systems require nanocrystalline core bars formed of many layers of laminated nanocrystalline ribbon to increase the effective area of the magnetic material [8].

Another method of reducing eddy current losses is fracturing, shown in Fig. 2(b), where the alloy is crushed into separate fragments bonded by the non-conductive adhesive. This technique further reduces the size of the eddy

current 'loops' or bulk electrical conductivity, leading to smaller eddy current losses. However, the bulk magnetic permeability will also be reduced, meaning the permeability of fractured nanocrystalline materials can be adjusted. Fracturing techniques are more unique to nanocrystalline materials, and current literature has demonstrated that the fracturing technique can significantly affect the resulting change in permeability, conductivity, and core loss. Standard fracturing techniques use a roller to produce a fracturing pattern, which is predominantly random, as illustrated in Fig. 2(b). Fractured and laminated nanocrystalline core materials have been shown to improve IPT system efficiency while reducing core volume and mass [6], [9]. A study in [10] compared rollers with 'dot' and 'square' features and found that the 'square' type roller produced greater uniformity and improved eddy current losses. An alternative method is presented in [11], here the roller produces uniform fracturing in the rolling direction, essentially creating another direction of lamination in the material and then the authors used two toroids with perpendicular lamination directions to account for the heavily anisotropic behavior which this introduces.

Due to their layered and heterogeneous construction, fractured and laminated nanocrystalline ribbons exhibit anisotropic electrical and magnetic properties. Since both the hysteretic and eddy current losses depend on the direction of the magnetic field, characterizing the core loss of nanocrystalline alloys in IPT systems is difficult. Thus far, analysis of IPT systems using nanocrystalline cores has been mostly limited to polarised Double-D (DD) couplers. A polarised field shape creates a horizontal flux component between the two poles of the coupler which significantly improves coupling and tolerance to misalignment. In a DD pad, this means the magnetic field is aligned with the core material in the 'flux pipe' as shown in Fig. 1(a) [3]. Shown in Fig. 1(b), the primary magnetic flux path of a DD IPT coupler involves sections of oblique magnetic flux angles (30°, 60°) that will have different core losses to the portion of the flux path aligned with the magnetic material (0°, blue) due to the impact of induced eddy currents at higher magnetic flux angles. Here, these portions with oblique flux are negligible compared to the primary flux path; hence, standard toroid measurements with aligned flux give reasonably accurate results. However, the anisotropic core loss is more difficult to predict in the design of non-polarised IPT magnetics, such as circular pads, due to the wider variation in field direction within the core. Hence, to accurately model more complex IPT systems using a nanocrystalline core, it is necessary to characterize the core loss dependence on magnetic flux angle.

Core loss measurements are conventionally made on toroidal cores using a classical two-winding method [12]. A toroid provides a closed magnetic circuit where the magnetic fields are completely aligned with the material in one dimension. Toroidal measurements on anisotropic nanocrystalline ribbons result in a significant error if the anisotropic properties of the material are ignored [13]. Loss measurements can be split into two categories: electrical and calorimetric.

Calorimetric measurements measure heat flow to determine the power dissipated in the system. These measurements are almost independent of frequency and excitation, bypassing the traditional electrical issue of phase discrepancy at higher frequencies [14]. Calorimetric measurements can then be further divided into transient and steady-state methods. Steady-state methods require the entire system to be at a thermal steady-state, which can take several hours for larger samples [15]. Transient measurements achieve similar accuracy by considering only the initial heating portion of the sample, reducing the required measurement time significantly [16]. This article uses a fluid-based hybrid steady-state and transient calorimetric method to determine the core loss of nanocrystalline ribbon samples.

The intention of this work is to present an anisotropic characterization method for nanocrystalline alloys used in IPT pad magnetics. This method improves anisotropic material evaluation for applications with nonaligned flux, such as in non-polarised IPT magnetics. The data measured using this method is intended to improve the core loss modelling of these magnetics in future work. The contributions of this article are listed as follows.

1) A novel method for characterizing a magnetic material's dependence on magnetic flux angle
2) A calorimetric method that combines the benefits of transient and steady-state measurements
3) A comparison of three nanocrystalline ribbons to determine the effect of fracturing on the angular dependence of nanocrystalline core loss in IPT systems operating at 85 kHz

Section II introduces the design of a magnetic setup for characterizing the angular dependence of core loss in magnetic materials. Section III describes the calorimetric method, introducing the principles of both steady-state and transient measurements and the proposed combination. Section IV compares three nanocrystalline samples using the proposed method. Finally, Section V concludes the manuscript.

II. ANISOTROPIC CHARACTERISATION METHOD
This section details the design of the magnetic structure for characterizing the nanocrystalline ribbons. The proposed method uses a Maxwell coil to generate a uniform magnetic field, within which the sample can be mechanically rotated to an angle θ and the coil current I_{coil} varied to determine the core loss at different magnetic flux angles and B. Fig. 3 shows a conceptual overview of the system.

A. ANISOTROPIC MAGNETIC PROPERTIES
To design the Maxwell coil and simulate the nanocrystalline sample, finite element analysis (FEA) simulation tools are used. FEA tools for the simulation of low-frequency magnetics require material properties such as magnetic permeability and electrical conductivity. For nanocrystalline-based magnetic composites, these magnetic properties are completely anisotropic and require detailed characterization before accurate simulations can be performed. The anisotropic bulk
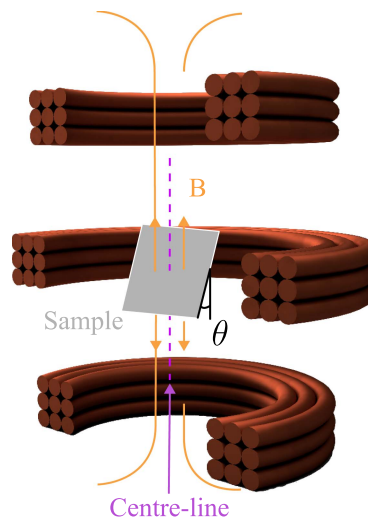

FIGURE. 3. Overview of magnetic excitation. A Maxwell coil generates a uniform magnetic field, and a nanocrystalline sample is rotated to measure core loss at different angles.
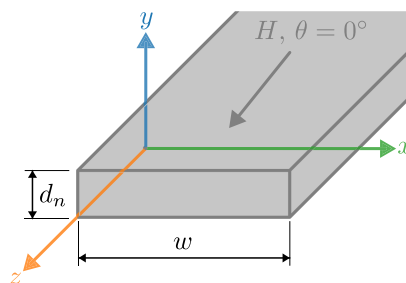

FIGURE. 4. Diagram of nanocrystalline ribbon construction showing only a single lamination layer of active material and material coordinate system.

material properties of the three-layer sample are determined based on the equations provided in [7]. The sample coordinate system is defined as shown in Fig. 4. The coordinate system is defined with the y axis in the lamination direction and the x and z-axes representing the transverse and rolling directions, respectively. The bulk electrical conductivity σ_x, σ_y and σ_z for each cartesian axis is calculated by,

$$\sigma_y = \frac{1}{F}\left(\frac{d_n}{w}\right)^2 \sigma \tag{1}$$

$$\sigma_x = \sigma_z = F\sigma \tag{2}$$

Where w is the width of a single layer and F is the stacking factor, calculated from the ratio of the thickness of the active volume to the thickness of the forming and adhesive layers. To determine the cross-sectional areas, optical microscopy, described in Section IV, was used to measure d_n and d_a as defined in Fig. 1(a). Typical values of d_n and d_a for the samples discussed in this work are approximately $20\,\mu$m and $5\,\mu$m. The anisotropic conductivity of the unlaminated nanocrystalline material after fracturing (σ) was measured at room temperature using a four-point Van der Pauw method with
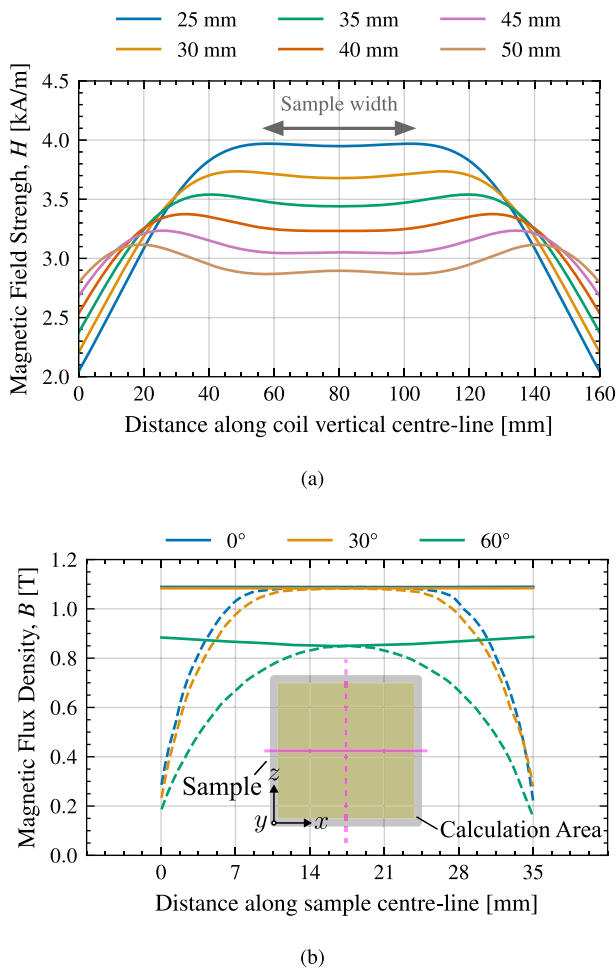
(a)

(b)

FIGURE. 5. (a) Simulated peak magnetic field strength H along the centre-line with varying values of g at I_{coil} = 20 A, 85 kHz, (b) Simulated magnetic flux distribution in a non-fractured sample across the vertical (z) and horizontal (x) centre-lines shown in the inset subfigure for θ = 0°, 30°, 60°.

a Keysight 34420A Micro-Ohm meter [17]. The anisotropic permeability of the sample is calculated similarly, using;

$$\mu_x = \mu_z = (1 - F)\mu_0 + F\mu_r \qquad (3)$$

$$\mu_y = \frac{\mu_r \mu_0}{F\mu_0 + (1 - F)\mu_r} \qquad (4)$$

Here, μ_0 is the permeability of vacuum, and μ_r is the relative permeability of the unlaminated nanocrystalline material, measured from a toroid using a partial cancellation method [14]. The calculations in (3) and (4) are repeated for every point of the measured B-H curve to determine the bulk B-H curve. The simulations presented in Fig. 5 and in Section III are performed using Ansys Maxwell. The sample is modelled as a lumped block model in all simulations with the same outer dimensions as the physical ribbon. The bulk B-H curve is defined by the nonlinear permeability curve calculated from (3) and (4). The conductivity is considered constant for each cartesian direction and calculated from (2) and (1). These material properties are defined using an 'object

coordinate system' with x, y and z defined as shown in Fig. 4. This ensures that as the sample is rotated, the definitions of the material properties are with respect to the sample and not the global coordinate system. Alternatively, the Maxwell coil could, equivalently, be rotated around a static sample.

Ansys Maxwell uses a proprietary automatic adaptive meshing FEA solver, which refines the tetrahedral mesh with each iteration. Since we are interested in the effect of eddy currents in the sample, the mesh sizing is critical. When solving for the eddy current distribution, the Ansys Maxwell documentation recommends a mesh with two elements per skin depth. Since the skin depth of these conductive nanocrystalline alloys is small ($\sim 20\,\mu$m for the non-fractured nanocrystalline), it gives a cell size of $\sim 10\,\mu$m. This results in a mesh with several million elements, requiring significant computational effort. However, the benefit of the proposed method is that this computational effort is only required to characterise the material. Once the material is characterized, IPT systems can be designed using a significantly coarser FEA mesh as the eddy current loss is included with the core loss using the proposed method. Simulations were performed with 20% refinement per pass and a percentage energy error of 1%.

B. MAGNETIC EXCITATION
To determine the core loss per volume of a given sample, the core loss needs to be approximately uniform throughout the sample volume. The hysteretic loss of the sample is proportional to the magnetic flux density, B; hence, a homogeneous magnetic field strength H is required to achieve a uniform core loss. Magnetic devices that create a uniform flux density distribution are commonly made of the material to be characterized, using an 'E' or 'U' type core or using easily predictable Mn–Zn ferrite cores such as single sheet testers for Fe–Si sheet characterization [18]. An air-core or coreless magnetic flux generation method is preferred to facilitate the rotation of the nanocrystalline sample.

A Maxwell coil is a magnetic structure designed to create a uniform magnetic field which consists of three coils stacked vertically and connected in series. The outer two coils are a matched pair as in a Helmholtz coil, and the centre coil has a larger radius as if the coils were placed on the surface of a virtual sphere [19]. As shown in Fig. 3, the Maxwell coil generates an approximately uniform magnetic field while a sample of nanocrystalline ribbon is held at an angle θ to the magnetic field. Based on the design methodology presented in [20], the outer coils are matched, and the radius of the centre coil is chosen based on a fixed ratio. Further design information can be found in [21].

The air gap g between each of the three coils was varied to select the final dimensions, as shown in Fig. 5(a). The field uniformity was assessed by comparing the difference between the maximum and minimum magnetic field strength within the sample region, ΔH. The values of ΔH for each value of g are given in Table 1. Here, g = 40 mm gives the lowest ΔH of ~ 5 A/m. Hence, g = 40 mm is selected, as the central region's magnetic field strength is most uniform.

TABLE 1. Variation of ΔH, the Difference Between the Maximum and Minimum Field Strength in the Sample Region, With the Gap Between Each Coil g

| g [mm]	25	30	35	40	45	50
ΔH [A/m]	14.7	19.2	14.6	5.1	7.2	20.1

The flat portion of the field strength in Fig. 5(a) is approximately 120 mm. The sample width should be less than one third this portion, i.e. under 40 mm. Smaller samples offer lower excitation current and a more uniform B distribution, especially at higher angles. However, the calorimetric measurements described in Section III require some minimum volume for the sample loss to be measurable. While nanocrystalline ribbon is typically produced in 65 mm wide samples, 35 mm was chosen as the final sample size to fit within the uniform field region while also considering the impact of the calorimetric measurements.

Fig. 5(b) shows how the magnetic flux density B varies across the sample in the vertical (solid lines) and horizontal (dashed lines) directions. In the vertical direction, the magnetic flux density is higher in the centre and approaches zero at the edge of the sample. In the horizontal direction, the magnetic flux density is mostly constant because the magnetic flux is perpendicular to the conductive nanocrystalline surface. As the sample is rotated (θ increases), the average magnetic flux density is reduced due to the increased effective cross-sectional area seen by the magnetic flux and the increasing opposing flux created by the induced eddy currents. The primary assumption of this method is that the magnetic flux angle agrees with the mechanical rotation of the sample. Initial simulations were performed to calculate the magnetic flux angle from the z axis, and these agree well with the assumption that the mechanical rotation is approximately equivalent to the rotation of the magnetic field.

Note that, in this work, the core loss is considered to be measured at the mean magnetic flux density $\overline{B}$ by taking the arithmetic mean of the magnetic flux density in the volume of a bounding box 1.5 mm from the edges of the sample (33.5 mm × 33.5 mm), shown as the yellow 'Calculation Area' in Fig. 5(b). This ensures that the calculated average magnetic flux density $\overline{B}$ is approximately equal to the peak magnetic flux density B_{pk}, i.e. $\Delta B \approx 0$, so that the core loss and B in the sample is approximately uniform.

III. CALORIMETRIC MEASUREMENT METHOD

The Maxwell coil discussed in Section II-B has ohmic losses, which are orders of magnitude larger than the expected core loss of the nanocrystalline sample. It is difficult to distinguish this loss from the desired core loss using electrical methods. As an example, a typical precision power analyzer such as the Yokogawa WT3000 measuring 25 W at 85 kHz would have an expected uncertainty of ±2.04 W, several times larger than the expected core loss [22].
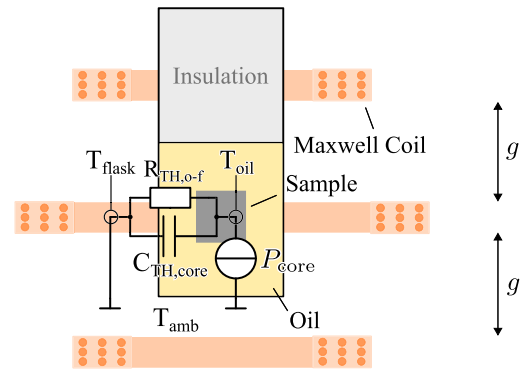
FIGURE. 6. Overview of calorimetric setup with overlayed equivalent thermal circuit and relevant temperature measurement points T_{amb}, T_{flask} and T_{oil}.

A. PROPOSED CALORIMETRIC METHOD
This article uses a fluid-based calorimetric measurement method to determine the core loss (P_{core}) induced by the designed Maxwell coil. A fluid-based method ensures that the temperature profile across the sample is uniform and provides a known heat capacity of the system (providing the fluid is well characterized) [23]. The proposed method combines steady-state and transient methods from the literature to overcome the issue of inaccurate calibration. In the following sections, the equations for both methods are derived, and the experimental setup used in this article is presented.

Fig. 6 shows a simple electrical analogy for the thermal behavior of the experimental setup. The interface between the outside of the flask and the nanocrystalline sample is modelled by a Cauer model where the thermal resistance and capacitance from the oil to flask $R_{\mathrm{TH,o\text{-}f}}$ and $C_{\mathrm{TH,core}}$ are in parallel. In general, steady-state methods calculate the energy required for a measured temperature rise ΔT from known material properties. Assuming there is no phase change, the heat added to the system (Q_{oil}) is classically determined from (5) [24].

$$Q_{\mathrm{oil}} = c_p m_{\mathrm{oil}} \Delta T \qquad (5)$$

Here, c_p is the specific heat at constant pressure of the oil, and m_{oil} is the mass of the oil used in the experiment. At steady-state, the thermal capacitance $C_{\mathrm{TH,core}}$ shown in Fig. 6 can be modelled as an open circuit. The heat flow lost from the system, $\dot{Q}_{\mathrm{loss}}$, can then be found from the temperature drop over $R_{\mathrm{TH,o\text{-}f}}$. P_{core} can then be found from the addition of the ideal calculation in (5) and the losses to the environment (Q_{loss}) over the period of the experiment (τ) as shown in (6).

$$P_{\mathrm{core}} = \frac{1}{\tau} \left(\underbrace{c_p m_{\mathrm{oil}} \Delta T}_{Q_{\mathrm{oil}}} + \underbrace{\int_0^{\tau} \frac{T_{\mathrm{oil}} - T_{\mathrm{flask}}}{R_{\mathrm{TH,o\text{-}f}}} dt}_{Q_{\mathrm{loss}}} \right) \qquad (6)$$

Here, T_{oil} and T_{flask} are the instantaneous values of the oil and flask temperature, respectively. In this work, ΔT is the

steady-state difference between the oil and flask temperatures, i.e. $\Delta T = T_{\text{OIL}} - T_{\text{FLASK}}$. Using the difference between these two temperatures accounts for the heating of the larger system by the Maxwell coil's ohmic losses, assuming the superposition principle applies [21]. To use (6), $R_{\text{TH,o-f}}$ must first be determined. Replacing the nanocrystalline sample with a power resistor, a known loss P_{cal} is produced in the calorimetric vessel to determine $R_{\text{TH,o-f}}$ from (7).

$$R_{\text{TH,o-f}} = \frac{T_{\text{OIL}} - T_{\text{FLASK}}}{P_{\text{cal}}} = \frac{\Delta T}{P_{\text{cal}}} \quad (7)$$

Here T_{OIL} and T_{FLASK} are the steady-state temperatures of the oil and flask respectively. The period τ can be very long for large values of the product $R_{\text{TH,o-f}} \cdot C_{\text{TH,core}}$, in the order of days for the materials used in this article. Hence, it is desirable to reduce the experiment time as much as possible, especially when considering multiple samples and several independent variables (θ, I_{coil}, T_{amb}). Transient methods consider only the initial portion of the temperature profile to determine core loss. During the initial portion of the experiment, the core losses of a sample can be approximated from only the terminal behavior of the effective thermal capacitance or heat capacity $C_{\text{TH,core}}$ by (8).

$$P_{\text{core}} = C_{\text{TH,core}} \frac{d}{dt}(T_{\text{oil}} - T_{\text{flask}}) = C_{\text{TH,core}} \frac{dT}{dt} \quad (8)$$

The rate of change of the rise in temperature of T_{oil} relative to T_{flask}, $\frac{d}{dt}(T_{\text{oil}} - T_{\text{flask}})$, is referred to as $\frac{dT}{dt}$. To determine the value of P_{core} from the measured $\frac{dT}{dt}$, the value of $C_{\text{TH,core}}$ needs to be accurately determined. In (6), the product $c_p m_{\text{oil}}$ is $C_{\text{TH,oil}}$, the heat capacity of the oil in the system, (6) assumes that $C_{\text{TH,oil}} >> C_{\text{TH,core}}$ and $C_{\text{TH,core}}$ can be ignored at steady-state. Conversely, (8) assumes that, in the first portion of the transient behavior, $C_{\text{TH,core}}$ dominates and hence $C_{\text{TH,oil}}$ is ignored. However, in a practical system, $C_{\text{TH,core}}$ is not constant and is non-linearly related to temperature, pressure and several other parameters as shown in (9). To avoid direct measurement of $C_{\text{TH,core}}$, as proposed in [25], a calibration curve is produced which allows the calculation of P_{core} directly from the measured value of $\frac{dT}{dt}$.

$$C_{\text{TH,core}} = f\left(c_p, T_{\text{oil}}, P_{\text{core}}, m_{\text{oil}}, R_{\text{TH,o-f}}\right) \quad (9)$$

As with the steady-state calculation, a known loss is typically produced electrically with an accurately measured DC source either from a power resistor [15] or using the core sample itself by determining its resistance from measured conductivity [16], [23]. This technique works well for Mn-Zn ferrites and other magnetic materials with low conductivity. However, the nanocrystalline ribbons of interest in this article have conductivities several orders of magnitude higher than Mn-Zn ferrites and, hence, require large DC currents to achieve significant losses for calibration. To induce a known loss in the system, samples of the nanocrystalline ribbon in the aligned position ($\theta = 0°$) use the steady-state measurements from (6) to determine the value of $\frac{dT}{dt}$ that corresponds to the measured temperature rise. In this way, the measured $C_{\text{TH,core}}$ consists
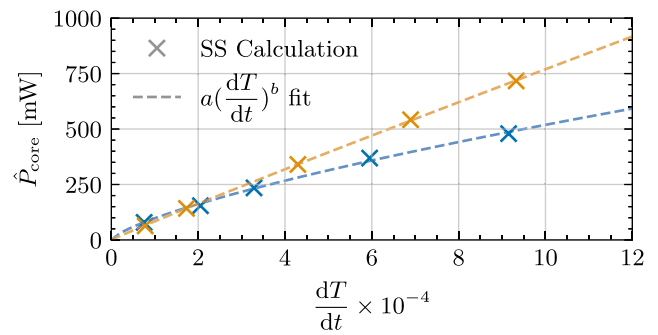

FIGURE. 7. Example calibration curves of measured rate of change of temperature $\frac{dT}{dt}$ to estimated core losses $\hat{P}_{\text{core}}$ for two different samples.

only of the surrounding oil, holder and the nanocrystalline ribbon sample without additional calibration equipment.

The aligned steady-state measurements are then fit with a curve of the form $a(\frac{dT}{dt})^b$, shown as a dashed line in Fig. 7. Here a and b are parameters determined by fitting steady-state loss measurements to the measured $\frac{dT}{dt}$ using a nonlinear least-squares technique [26]. Hence, the core loss can be directly determined from a measured value of $\frac{dT}{dt}$ by,

$$\hat{P}_{\text{core}} = a\left(\frac{dT}{dt}\right)^b \quad (10)$$

Initially (assuming $t = 0$ is when the excitation begins), the measured $\frac{dT}{dt} = 0$ due to transport delay, fluid transfer mechanics and the thermal capacitance of the temperature sensor. For $t > 0$, $\frac{dT}{dt}$ climbs to a maximum before returning to 0 when the system reaches a steady state. When $\frac{dT}{dt}$ is maximum, the impact of heat dissipation is minimum and hence (8) is most valid. As such, the value of $\frac{dT}{dt}$ in (8) and (10) is chosen to be max $\frac{dT}{dt}$.

Fig. 8 provides an overview of each step of the characterization method. The temperature of the oil (T_{oil}) and flask (T_{flask}) is measured for each desired value of I_{coil} and θ for each material. The measured temperature values are then filtered and the difference is differentiated to find the maximum value of $\frac{dT}{dt}$. Based on a calibration curve determined from the maximum measured $\frac{dT}{dt}$ for the samples in the aligned position ($\theta = 0$), and the steady-state core loss P_{core} at the corresponding $\overline{B}$ as predicted by FEA, the core loss P_{core} for each experiment is determined.

B. EXPERIMENTAL SETUP

Fibre Bragg Grating (FBG) sensors were used for temperature measurement because magnetic fields do not affect the optical fibres [27]. The positions of the FBG sensors are shown as T_{oil}, T_{flask}, and T_{amb} in Fig. 6. Luna os4310 non-metallic FBG sensors are measured with a Luna HYPERION si255 optical sensing interrogator, which offers temperature accuracies below 0.2 °C. All temperature measurements were sampled at 1 kHz then resampled to 1 Hz before being filtered with a low pass filter to reduce the prominent temperature variation due
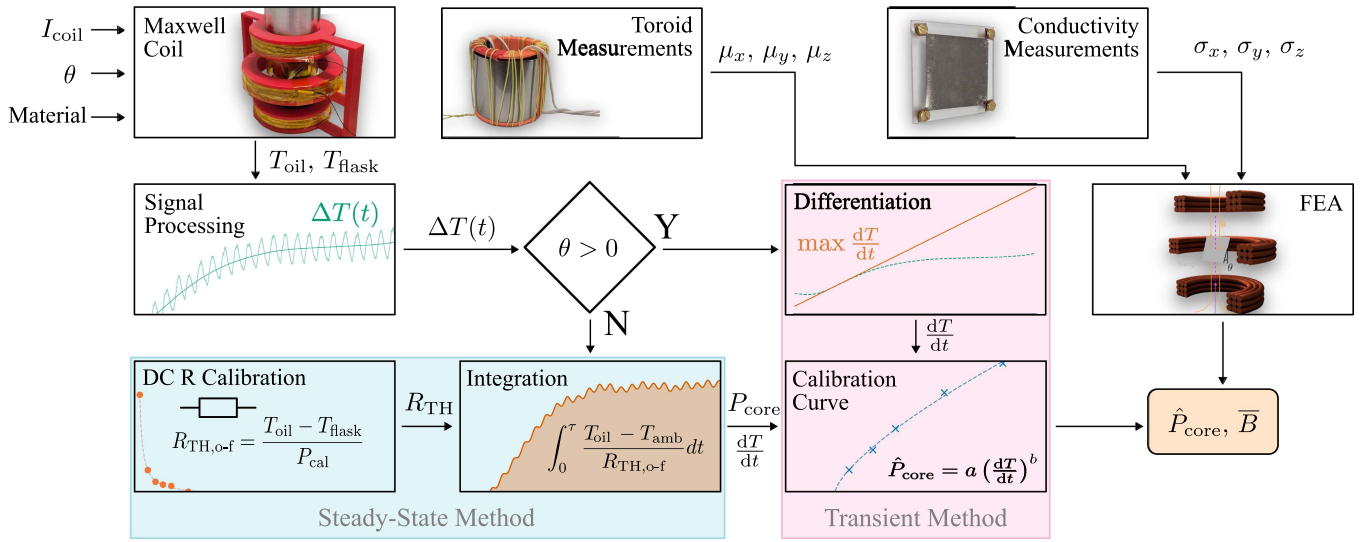
FIGURE. 8. Overview of characterization method, a steady-state calorimetric method is used for the aligned ($\theta = 0$) measurements, which are used to calibrate the transient calorimetric measurement used for each of the nonaligned ($\theta > 0$) measurements.
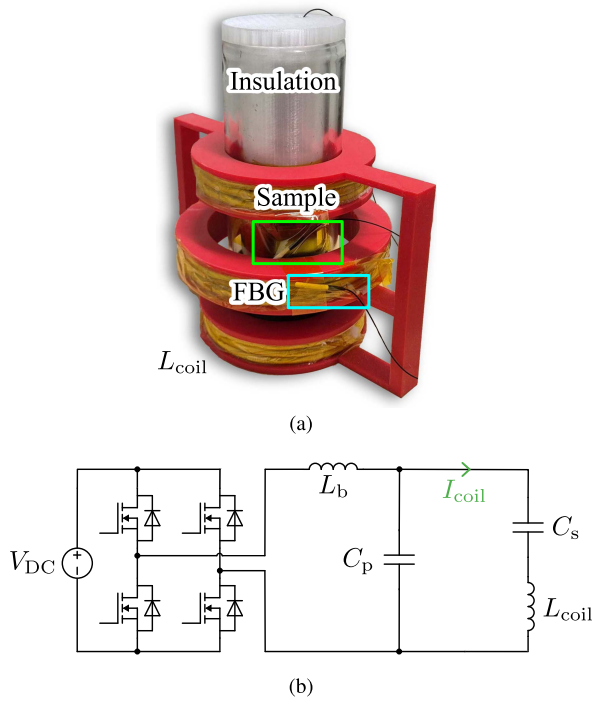

(a)

(b)

FIGURE. 9. (a) Annotated picture of experimental setup, (b) Schematic of electrical excitation.

TABLE 2. System Parameters

Parameter	Value	Parameter	Value
f	85 kHz	T_{amb}	18 °C to 20 °C
L_{coil}	52.14 µH	c_p	1.9 kJ kg^{-1} K^{-1}
L_b	37.5 µH	m_{oil}	107.6 g to 121.1 g
C_p	93.62 nF	$R_{TH,o\text{-}f}$	27.5 K W^{-1}
C_s	239.13 nF	θ	0° to 60°
V_{DC}	$\leq$600 V	V_{core}	0.066 15 m^3

3D-printed PETG cap filled with fibreglass insulation material to minimize leakage through the top of the flask. The sample holder is part of the PETG cap to minimize its effect on the system's effective heat capacity. Still, its impact on the thermal behavior was accounted for empirically in the curve fitting process of (10). Note that the protective layer of PET is removed on both sides of the nanocrystalline sample before the experiment. MOBILTHERM 605 [29], a heat transfer mineral oil, ensures a uniform sample temperature profile.

The Maxwell coil was compensated with an LCCL network and energized with a full-bridge inverter as shown in Fig. 9(b). The component values and other parameters are detailed in Table 2. The coil current was controlled by varying the input DC voltage using a Python script to maintain the desired $\bar{B}$ in the sample. Coil currents were chosen to give an appropriate step size in $\bar{B}$ for each sample but were limited by the ohmic heating of the Maxwell coil's litz wire. Steady-state measurements were run for a period of 8.33 h and then allowed to cool for 16.66 h, resulting in a period of 25 h. For the transient measurements, each current level was run until the second derivative of the temperature rise ($\frac{d^2T}{dt^2}$) reached 0 (NB: first derivative is maximum), which correlates

to the environmental chamber control system. The $T_{oil} - T_{flask}$ temperature profile was then filtered with a Savitsky-Golay filter to further eliminate measurement noise [28].

Fig. 9(a) shows the experimental setup for the proposed Maxwell coil method. To meet the desired dimensions, the Maxwell coil is wound on a 3D-printed coil former. A custom borosilicate glass vacuum flask ensures a high thermal impedance $R_{TH,o\text{-}f}$. The flask is plugged from above with a

TABLE 3. Material Properties

Sample	Fe %	Cu %	Nb %	Si %	B %	μ_r	σ_x	σ_y	σ_z	B_{sat}	C'_m ($\times 10^7$)	y	z
F_{700}	79.4	1.0	3.3	16.3	~ 0	700	38.2 kS m^{-1}	0.06 S m^{-1}	4.78 kS m^{-1}	1.2 T	1.04	1.85	0.81
F_{2000}	87.5	1.3	3.8	7.4	~ 0	2000	32.0 kS m^{-1}	0.04 S m^{-1}	96.0 kS m^{-1}	1.4 T	1.63	1.67	1.08
N_{12000}	79.4	1.0	3.3	16.3	~ 0	12000	650 kS m^{-1}	0.28 S m^{-1}	650 kS m^{-1}	1.2 T	1.72	2.06	0.95

to a period of ~ 2.22 h for each angle and excitation current. Between each experiment, the system was allowed to cool to the controlled ambient temperature of $\sim 20\,°C$. After it had cooled, the sample could then be changed, rotated or repeated at a different coil current.

IV. CORE LOSS RESULTS

This section presents the measured core loss of samples of three commercially available three-layer nanocrystalline ribbons from AE&M, a non-fractured ribbon (N_{12000}), and two fractured ribbons of different permeability (F_{700}, F_{2000}). F_{2000} is only fractured on one side. Hence, the three-layer F_{2000} sample contains one layer of fractured material and two non-fractured layers with higher conductivity and permeability. The material properties of each sample are detailed in Table 3. The provided weight percentage elemental composition was determined from the average composition of 5 samples measured with Energy Dispersive Spectroscopy (EDS) and indicates that the F_{2000} sample is of a different composition to F_{700} and N_{12000}. The difference in composition is demonstrated by the higher saturation flux density B_{sat} and hysteretic loss. Results from the proposed method are compared with toroid measurements to verify the method's accuracy in the aligned position, and comparisons are made between the different levels of fracturing.

A. COMPARISON WITH TOROID MEASUREMENTS

In the aligned position ($\theta = 0\,°$), the magnetic flux is aligned with the material in the rolling direction, and the core loss is almost entirely hysteretic, i.e. the same as measured in a toroid. The empirical Steinmetz equation is used to model the core loss per unit volume P_V given by (11). Where C_m, x and y are coefficients determined from numerically fitting the curve to the experimentally measured core loss known as the Steinmetz coefficients of the material [30]. For fixed frequency operation at 85 kHz, $C_m f^x$ can be simplified as a constant C'_m.

$$P_V = C_m f^x B^y = C'_m B^y \qquad (11)$$

The estimated hysteretic core loss $\hat{P}_{core}$ can then be determined from (11) by,

$$\hat{P}_{core} = P_V \times V_{core} = C'_m B^y V_{core} \qquad (12)$$

Where V_{core} is the total active volume of the ribbon sample. The Steinmetz coefficients for each sample were measured on a toroid of the core material using a partial cancellation method as detailed in previous work [14], [31]. The measured
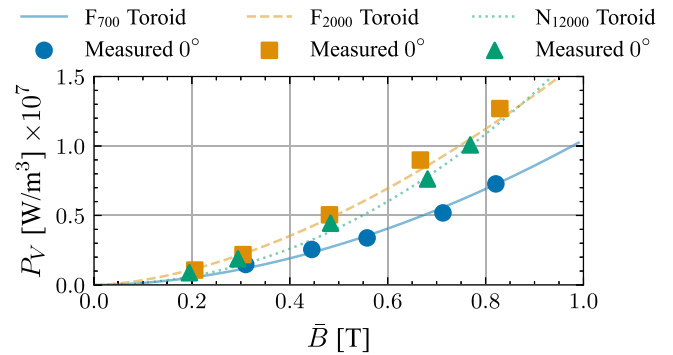

FIGURE. 10. Measured core loss for each sample in the aligned position with the proposed method and a toroid of the same material.
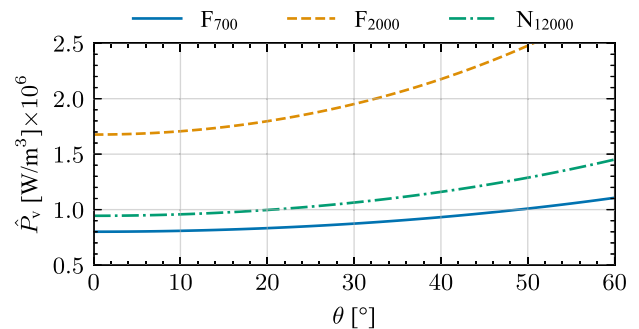

FIGURE. 11. Calculated loss density for each material from fitted ADSE at 200 mT for varying magnetic flux angle θ.

core loss with the proposed method is compared to (12) in Fig. 10, with a maximum relative error of 14.98%.

B. EFFECTS OF INCREASING MAGNETIC FLUX ANGLE

Fig. 11 shows how the measured core loss changes at magnetic flux angles of $30\,°$, $60\,°$ compared to the same measured core loss at $0\,°$ for the N_{700} ribbon. As the flux angle increases, the measured core loss is higher for the same $\bar{B}$. This article proposes a modified angle-dependent Steinmetz equation (ADSE) given in (13) to model this behavior.

$$P_V = C'_m B^y \cosh(z \cdot \theta) \qquad (13)$$

The additional term $\cosh(z \cdot \theta)$ is fitted with a nonlinear least squares technique with the C'_m and y parameters calculated by nonlinear least squares when fitting toroid data to (11). In this way, the proposed ADSE models the material's behavior as it is rotated in a uniform magnetic field or, equivalently, as the magnetic field is rotated around the sample. When $\theta = 0$, $\cosh(z \cdot \theta) = 1$ and hence the model is equal to the hysteretic behavior described by (11) when determined from a toroid.
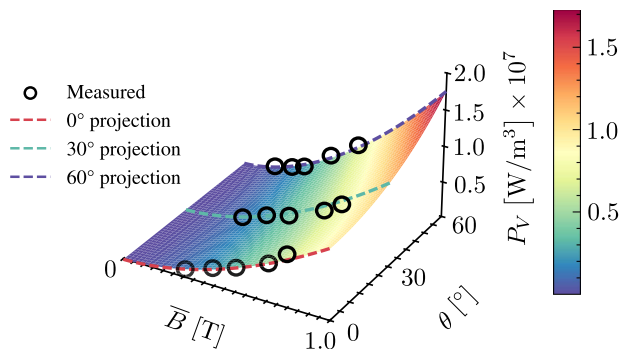
FIGURE. 12. Measured core loss vs $\bar{B}$ for F_{700} at magnetic flux angle θ values of $0°$, $30°$ and $60°$ on a linear scale with fitted ADSE surface

This means the unmodified parameters provided in Table 3 can be used for aligned fields in existing FEA software without the proposed z parameter. As θ increases, the impact of eddy currents means the total core losses increase for the same B, increasing core loss exponentially. The function $\cosh(z \cdot \theta)$ was chosen because it describes the above behaviour well, but for other materials, any function $f(\theta)$ could modify the Steinmetz equation to produce an ADSE. Fig. 12 shows a fitted surface of the ADSE for F_{700}, the fitted surface has a maximum mean relative error of 32.4% for the three materials considered in this article. This error occurs for the partially fractured F_{2000}, which is likely due to the assumption of uniform B in the calculation of $\bar{B}$. As $\theta \rightarrow 90°$, the ADSE error increases significantly as the model cannot predict P_{core} when B is 0 ($0^y = 0$). However, a higher value of the fitted parameter z from (13) indicates a greater dependence on the magnetic flux angle θ and hence is a useful indicator for performance in IPT systems with nonaligned fields.

C. INFLUENCE OF FRACTURING

Fig. 13 shows optical microscope captures of each of the samples considered in this article. These images are captured with an Olympus DSX1000 digital microscope at 50X magnification and composited with Olympus PRECiV DSX imaging software. The images are further processed using a Laplacian image gradient filter from OpenCV. This filter highlights rapid changes in the image, meaning the fracture lines in the micrographs of F_{700} and F_{2000} are more easily visible. Each image in the figure is approximately $1000\,\mu m$ wide, allowing for easy comparison of the fracture sizing. From these images, the extent of fracturing significantly differs between each sample. F_{700} has the smallest fragments, in the order of $10\,\mu m$ to $50\,\mu m$, in contrast, F_{2000}'s fragments are larger than $100\,\mu m$.

The right images of Fig. 13 show the core loss per unit volume of each sample for angles of $0°$, $30°$ and $60°$. F_{700} has the lowest core loss in the aligned position (as indicated in Fig. 10) and increases less with greater θ as illustrated by the lowest value of z. The lower permeability of F_{700} and F_{2000} mean it is difficult to reach higher values of B, requiring high

values of I_{coil} and as such $\bar{B}$ for each sample is limited to $0.8\,T$ to $1\,T$.

N_{12000} is the non-fractured sample and hence has the highest conductivity in each direction, resulting in a higher z value than the fractured sample of this material and a $\sim 250\%$ increase in core loss per unit volume in the $60°$ position compared to the aligned position. Fig. 13(e) shows the unfractured surface of N_{12000}. Visible markings can be seen of the production process on the surface, indicating the rolling direction. These markings are also visible in Fig. 13(a) but are harder to see due to the adhesive layer that covers all three samples.

F_{2000} demonstrates the highest initial core loss, and its losses increase significantly with θ due to the higher σ_z, resulting in the highest z value. Fig. 13(d) show the material's B-P curve, initially at the lowest $\bar{B}$ the $60°$ measurements shows some overlap with the $30°$ due to the measured absolute core loss being below $25\,mW$ and the measurement error increasing significantly. The measured core loss of F_{2000} increases significantly for $\theta = 60°$, resulting in the largest z despite the fracturing of the top layer. The partially fractured F_{2000} contains primarily non-fractured material, meaning the bulk conductivity as shown in Table 3, which was measured on the fractured side, is likely higher in reality. However, the maximum $\bar{B}$ for the $60°$ measurement is only $\sim 0.6\,T$, limited by the heating of the Maxwell coil.

F_{700} and N_{12000} show the measured core loss 'lifting' away from the hysteretic behavior ($\theta = 0$) at approximately half the saturation flux density (B_{sat}), for F_{2000} this would occur at $\sim 0.7\,T$. The measured points for F_{2000} show a step change in loss density, which occurs only for the partially fractured material. Based on this behavior, F_{2000} has a high z value and is not an ideal material for IPT applications due to its higher hysteretic loss than N_{12000} and F_{700}.

D. MATERIALS SELECTION FOR IPT

The composition of F_{700} and N_{12000} looks to be more suitable than the composition of F_{2000}. Based on these results, F_{700} has the lowest overall core loss and the lowest z. Higher permeability is not of significant benefit in typical IPT magnetics due to the large air gap between the pads. Thus from these three materials, F_{700} looks preferable. However, N_{12000}'s z parameter is only 17.3% higher without the added expense of fracturing the material. It then depends on the application and cost limitations for which material is the most suitable.

Compared to TDK N95 Mn–Zn ferrite (a loss density of $\sim 400\,kW/m^3$), the measured loss density in the aligned position at $100\,mT$ is 411% higher for F_{2000}, 176% higher for N_{1200} and 173% higher for F_{700}. Note that this article is focused on the proposed measurement technique; the materials evaluated are those that are currently commercially available. Literature has demonstrated nanocrystalline alloys that have loss densities as good as or better than ferrite at $85\,kHz$ [31]. In addition, the benefits of nanocrystalline alloys come largely from thermal and mechanical improvements over ferrites, as discussed in Section I.
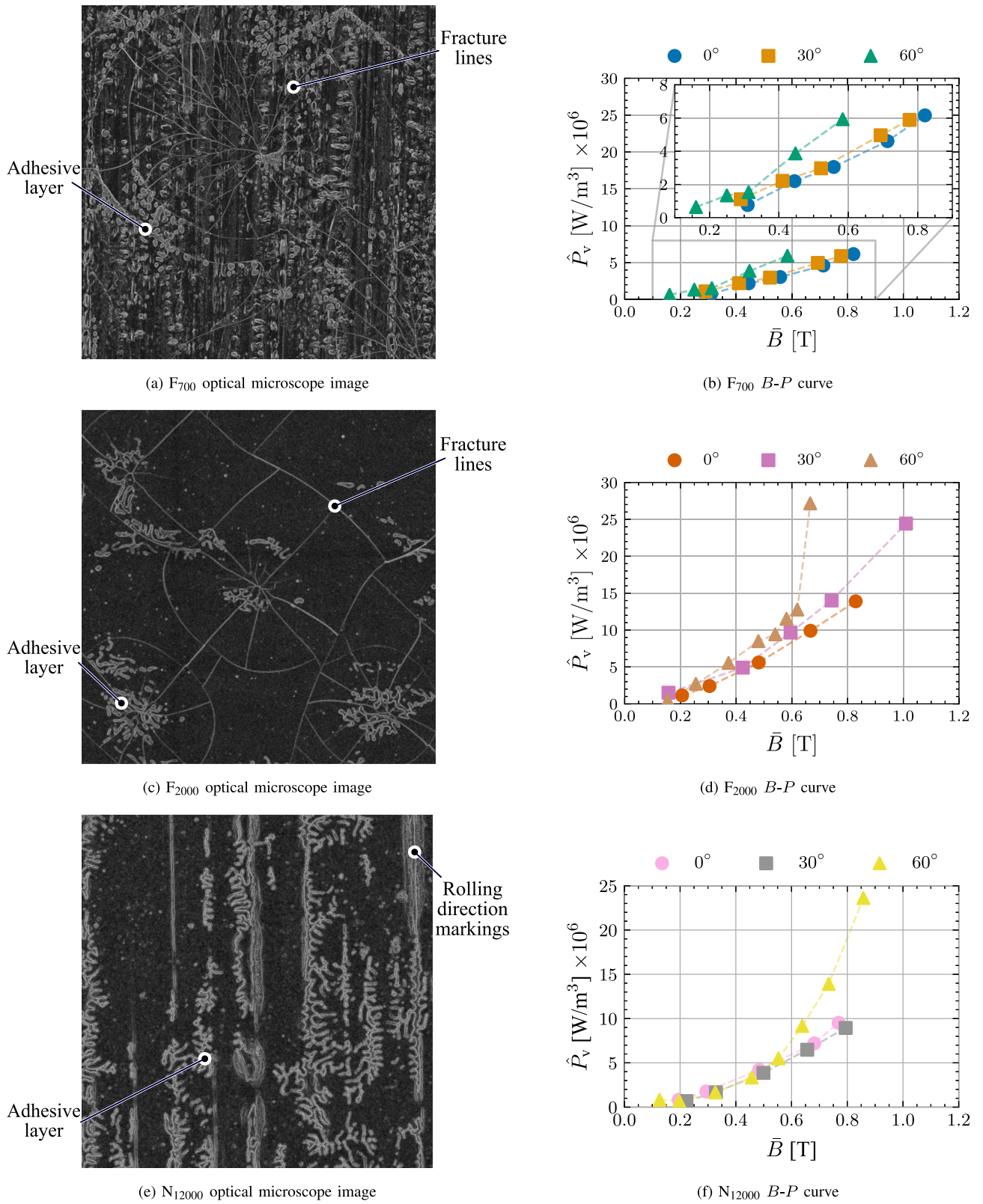
(a) F$_{700}$ optical microscope image

(b) F$_{700}$ B-P curve

(c) F$_{2000}$ optical microscope image

(d) F$_{2000}$ B-P curve

(e) N$_{12000}$ optical microscope image

(f) N$_{12000}$ B-P curve

FIGURE. 13. Optical microscope images with 1000 μm scale and measured core loss per unit volume $\hat{P}_V$ against mean flux density $\bar{B}$, for flux angle $\theta \in [0\,°, 30\,°, 60\,°]$ for each of the measured samples, F$_{700}$, F$_{2000}$ and N$_{12000}$.

V. CONCLUSION

This paper has proposed a novel method for characterizing the anisotropic core loss of nanocrystalline ribbons in the context of inductive power transfer (IPT) systems. A Maxwell coil was designed to create a uniform 85 kHz magnetic field, which induces a core loss in a sample of nanocrystalline alloy. A hybrid transient and steady-state calorimetric method was used to extract the measured core loss, which reduced the time required for a measurement from 25 h to $\sim$ 2.22 h. This method replaces the typical transient DC calibration method with steady-state calorimetric measurements, allowing for the measurement of materials with high electrical conductivity.

The proposed method was used to compare three different nanocrystalline samples: one non-fractured, one partially fractured, and one fractured material. The non-fractured material shows an increase of up to 250% in core loss for misaligned fields, while the fractured material increases by only 140%. To model the angular dependency of these materials, a modified angle-dependent Steinmetz equation is proposed, which introduces a z-parameter that indicates a material's dependence on magnetic flux angle. The material with the greatest degree of fracturing showed the lowest z value, indicating it is more suitable for IPT systems with nonaligned fields.

ACKNOWLEDGMENT

REFERENCES

[1] T. R. Hawkins, O. M. Gausen, and A. H. Strømman, "Environmental impacts of hybrid and electric vehicles—a review," *Int J. Life Cycle Assess*, vol. 17, no. 8, pp. 997–1014, 2012.

[2] G. A. Covic and J. T. Boys, "Inductive power transfer," *Proc. IEEE*, vol. 101, no. 6, pp. 1276–1289, Jun. 2013.

[3] M. Budhia, J. T. Boys, G. A. Covic, and C.-Y. Huang, "Development of a single-sided flux magnetic coupler for electric vehicle IPT charging systems," *IEEE Trans. Ind. Electron.*, vol. 60, no. 1, pp. 318–328, Jan. 2013.

[4] P. A. J. Lawton, F. J. Lin, and G. A. Covic, "Magnetic design considerations for high-power wireless charging systems," *IEEE Trans. Power Electron.*, vol. 37, no. 8, pp. 9972–9982, Aug. 2022.

[5] "SIFERRIT material N95 datasheet," *TDK Electron. AG*, Feb. 2023.

[6] M. Xiong, X. Wei, Y. Huang, Z. Luo, and H. Dai, "Research on novel flexible high-saturation nanocrystalline cores for wireless charging systems of electric vehicles," *IEEE Trans. Ind. Electron.*, vol. 68, no. 9, pp. 8310–8320, Sep. 2021.

[7] J. Wang, H. Lin, Y. Huang, and X. Sun, "A new formulation of anisotropic equivalent conductivity in laminations," *IEEE Trans. Magn.*, vol. 47, no. 5, pp. 1378–1381, May 2011.

[8] D. E. Gaona, S. Ghosh, and T. Long, "Feasibility study of nanocrystalline-ribbon cores for polarized inductive power transfer pads," *IEEE Trans. Power Electron.*, vol. 35, no. 7, pp. 6799–6809, Jul. 2020.

[9] Y. Wang, C. Q. Jiang, C. Chen, X. Wang, X. Li, and T. Long, "Design and analysis of inductive power transfer system using nanocrystalline flake ribbon core," *IEEE J. Emerg. Sel. Topics Power Electron.*, vol. 12, no. 4, pp. 3334–3347, Aug. 2024.

[10] C. Chen, C. Q. Jiang, T. Ma, B. Zhang, J. Xiang, and J. Zhou, "Core loss optimization for compact coupler via square crushed nanocrystalline flake ribbon core," *IEEE Trans. Power Electron.*, vol. 39, no. 8, pp. 9095–9099, Aug. 2024.

[11] Z. Luo, X. Li, C. Jiang, Z. Li, and T. Long, "Permeability-adjustable nanocrystalline flake ribbon in customized high-frequency magnetic components," *IEEE Trans. Power Electron.*, vol. 39, no. 3, pp. 3477–3485, Mar. 2024.

[12] C. Xiao, G. Chen, and W. G. H. Odendaal, "Overview of power loss measurement techniques in power electronics systems," *IEEE Trans. Ind. Appl.*, vol. 43, no. 3, pp. 657–664, May/Jun. 2007.

[13] Y. Wang, G. Calderon-Lopez, and A. J. Forsyth, "High-frequency gap losses in nanocrystalline cores," *IEEE Trans. Power Electron.*, vol. 32, no. 6, pp. 4683–4690, Jun. 2017.

[14] D. Hou, M. Mu, F. C. Lee, and Q. Li, "New high-frequency core loss measurement method with partial cancellation concept," *IEEE Trans. Power Electron.*, vol. 32, no. 4, pp. 2987–2994, Apr. 2017.

[15] S. Coday and R. C. N. Pilawa-Podgurski, "Characterization and modeling of ceramic capacitor losses under large signal operating conditions," *IEEE Open J. Power Electron.*, vol. 4, pp. 24–33, 2023.

[16] P. Papamanolis, T. Guillod, F. Krismer, and J. W. Kolar, "Transient calorimetric measurement of ferrite core losses up to 50 MHz," *IEEE Trans. Power Electron.*, vol. 36, no. 3, pp. 2548–2563, Mar. 2021.

[17] L. Sun, S. S. Park, D. Sheberla, and M. Dincă, "Measuring and reporting electrical conductivity in metal–organic frameworks: Cd $_2$ (TTFTB) as a case study," *J. Amer. Chem. Soc.*, vol. 138, no. 44, pp. 14772–14782, 2016.

[18] S. Aihara, H. Shimoji, T. Todaka, and M. Enokizono, "Measurement of local vector magnetic properties in laser scratched grain-oriented silicon steel sheet with a vector-hysteresis sensor," *IEEE Trans. Magn.*, vol. 48, no. 11, pp. 4499–4502, Nov. 2012.

[19] J. C. Maxwell, *A Treatise on Electricity and Magnetism*. Oxford, U.K.: Clarendon Press, 1873.

[20] B. Mihailescu, I. Plotog, and M. N. Velcea, "Comparative assessment of maxwell and helmholtz coils magnetic field for biotechnological applications," in *Proc. IEEE 21st Int. Symp. Des. Technol. Electron. Packag.*, 2015, pp. 157–160.

[21] A. K. Bailey, W. Zhang, S. Kim, and G. A. Covic, "Calorimetric measurement of losses in nanocrystalline cores," in *Proc. 2024 IEEE Wireless Power Technol. Conf. Expo*, 2024, pp. 69–73.

[22] "Yokogawa WT 5000 precision power analyzer," Yokogawa Test & Measurement Corporation. [Online]. Available: https://tmi.yokogawa.com/nz/solutions/products/power-analyzers/wt5000/

[23] J. Reynvaan, M. Pajnić, and J. Krenn, "Evaluating fluid based transient calorimetric method for measurement of the ferrite core losses," in *Proc. 11th Int. Conf. Power Electron. ECCE Asia*, 2023, pp. 3308–3313.

[24] M. J. Moran, H. N. Shapiro, D. D. Boettner, and M. B. Bailey, *Fundamentals of Engineering Thermodynamics*, 9th ed. Hoboken, NJ, USA: Wiley, 2018.

[25] V. Loyau, M. LoBue, and F. Mazaleyrat, "Comparison of losses measurement in a ferrite with two calorimetric methods," *IEEE Trans. Magn.*, vol. 46, no. 2, pp. 529–531, Feb. 2010.

[26] D. W. Marquardt, "An algorithm for least-squares estimation of nonlinear parameters," *J. Soc. Ind. Appl. Math.*, vol. 11, no. 2, pp. 431–441, 1963.

[27] Q. Wang, Z. Fen, F. Deng, G. Huang, L. Yan, and Y. Dai, "Fiber bragg gratings for strain sensing in high temperature superconducting magnet," *IEEE Trans. Appl. Supercond.*, vol. 17, no. 2, pp. 2377–2380, Jun. 2007.

[28] A. Savitzky and M. J. E. Golay, "Smoothing and differentiation of data by simplified least squares procedures," *Anal. Chem.*, vol. 36, no. 8, pp. 1627–1639, 1964.

[29] "Mobiltherm 605 datasheet," *Exxonmobil*, 2022.

[30] C. Steinmetz, "On the law of hysteresis," *Proc. IEEE*, vol. PROC-72, no. 2, pp. 197–221, Feb. 1984.

[31] W. Zhang, S. Kim, D. J. Thrimawithana, G. A. Covic, L. Zhao, and Z. Li, "Nanocrystalline core loss in high power IPT systems for EV charging applications," in *Proc. 2024 IEEE Wireless Power Technol. Conf. Expo*, 2024, pp. 154–158.
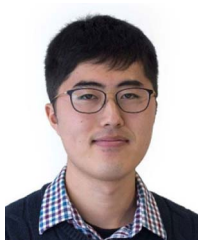
ALEXANDER K. BAILEY (Student Member, IEEE) received the B.E. (Hons.) degree in electrical and electronics engineering in 2024, from The University of Auckland, Auckland, New Zealand, where he is currently working toward the Ph.D. degree. His research interests include wireless power transfer, multiphysics modelling and power electronics.

WENTING ZHANG (Graduate Student Member, IEEE) received the B.S. degree in electrical engineering and its automation from North China Electric Power University, Baoding, China, in 2018, and the M.E. degree in electrical engineering from the Hebei University of Technology, Tianjin, China, in 2022. She is currently working toward the Ph.D. degree in electrical and electronics engineering with the University of Auckland, Auckland, New Zealand. Her research interests include wireless power transfer for EV charging, magnetic materials and applications.

SEHO KIM (Member, IEEE) received the B.E. (Hons.) and Ph.D. degrees in electrical and electronics engineering from The University of Auckland, Auckland, New Zealand, in 2012 and 2018, respectively. He is currently a Senior Lecturer with the Power Electronics Group, Department of Electrical, Computer, and Software Engineering, The University of Auckland. His research focuses on the design of inductive power transfer systems for charging electric vehicles.

GRANT A. COVIC (Senior Member, IEEE) received the B.E. (Hons.) and Ph.D. degrees in electrical and electronic engineering from The University of Auckland (UoA), Auckland, New Zealand, in 1986 and 1993, respectively. He was appointed as a full time Lecturer in 1992, Senior Lecturer in 2000, Associate Professor in 2007, and Professor in 2013 with the Department of Electrical, Computer, and Software Engineering, UoA. In 2010, he cofounded (with Prof. John Boys) a new global startup company "HaloIPT" focusing on electric vehicle (EV) wireless charging infrastructure, which was sold in late 2011. He is currently the Head of inductive power research with the UoA and is directing a government funded research program on stationary and dynamic wireless charging of EVs within the road, while also coleading the interoperability subteam within the SAE J2954 wireless charging standard for EVs. He holds a number of patent families with many more pending, from which licenses in specialized application areas of inductive power transfer (IPT) have been granted around the world. He has authored or coauthored more than 200 refereed papers in international journals and conferences in the areas of his research interests which include power electronics, EV battery charging, and resonant IPT. Dr. Covic is a Fellow of Engineering New Zealand and Royal Society of New Zealand. He was the recipient of the Clean Equity Monaco Award for excellence in the field of environmental engineering, during this time at HaloIPT, two NZ Clean Innovation Awards in the emerging innovator and design and engineering categories, New Zealand Prime Minister's Science Prize, Vice Chancellors commercialization medal, and KiwiNet Research commercialization Awards for scientific research, which has seen outstanding commercial success. He was a Distinguished Lecturer for the IEEE Transportation Electrification Community, from 2016 to 2019. He is currently active on the steering committee for wireless power week.